Effects of Ta substitution on the microstructure and transport properties of Hf-doped NbFeSb half-Heusler thermoelectric materials

Nader Farahi [a,], Christian Stiewe[a], D. Y. Nhi Truong[a], Yixuan Shi[b], Soma Salamon[c], Joachim Landers[c], Benedikt Eggert[c], Heiko Wende[c], Johannes de Boor[a], Holger Kleinke[b], and Eckhard Müller[a,d]*

[a] Institute of Materials Research, German Aerospace Center (DLR), D-51170 Köln, Germany

[b] Department of Chemistry and Waterloo Institute for Nanotechnology, University of Waterloo, Waterloo, Ontario N2L 3G1, Canada

[c] Faculty of Physics and Center for Nanointegration Duisburg-Essen (CENIDE), University of Duisburg-Essen, Lotharstr. 1, 47057 Duisburg, Germany

[d] Institute of Inorganic and Analytical Chemistry, Justus Liebig University Gießen, Heinrich-Buff-Ring 17, D-35392 Gießen, Germany

*Corresponding author contact information: nfarahi@uwaterloo.ca

Keywords: thermoelectric, half-Heusler, antimonide, alloying, doping

ABSTRACT. This investigation demonstrates the effect of partial substitutions of Nb by refractory Ta on the microstructure and thermoelectric properties of Hf-doped NbFeSb materials. All the synthesized samples show a heavily doped semiconducting character with the electrical conductivity higher than 3500 $\Omega^{-1}cm^{-1}$ at 326 K. Furthermore, the samples containing Ta display consistently lower (~ 10% - 13%) thermal conductivity of ~ 7 W $m^{-1}K^{-1}$ at 350 K compared to a value of ~ 8 W $m^{-1}K^{-1}$ at the same temperature for the non-substituted sample. The vivid impact of Ta substitutions on reducing the lattice thermal conductivity of NbFeSb based materials is chiefly due to the lattice disorder originating from the mass difference between Ta and Nb atoms, resulting in ~ 28% reduction in lattice thermal conductivity of the $Nb_{0.73}Hf_{0.12}Ta_{0.15}FeSb$ sample at 350 K compared to the non-substituted sample. The results of our Mößbauer spectroscopy measurements exclude the possibility of mixed Fe occupancies. Although magnetic properties were not strongly modified by the Ta substitution, $Nb_{0.83}Hf_{0.12}Ta_{0.05}FeSb$ shows a magnetic phase transition at ~ 150 K, which is not observed in $Nb_{0.88}Hf_{0.12}FeSb$. This could be caused by extrinsic defects and microstructure induced by Ta addition. All samples exhibit a similar maximum dimensionless figure of merit value, zT_{max}, of ~ 0.75 at 800 K, which is comparable to the high efficiency materials previously reported in this system and makes them potential candidates to be utilized as *p*-type legs in half-Heusler based thermoelectric generators (TEG).

1. Introduction

Considering the destructive influence of climate change on our ecosystem; there is a tremendous need for technologies that can minimize the consumption of fossil fuels, thus reducing CO_2 emission. Since a considerable amount of energy produced by fossil fuels in

industry is lost as waste heat, it is crucial to be able to retrieve as much waste energy as possible. Almost all industrial processes require electricity for operations; therefore, converting waste heat into electricity is among the best possible scenarios. In that theme, thermoelectric (TE) materials are invaluable due to their unique characteristics of converting heat directly into electricity. To utilize these materials in waste heat recovery for stationary[1] and non-stationary[2] industrial applications, both high thermal and mechanical stability as well as high efficiency are required.[3–5] To assess the efficiency of a thermoelectric material, its figure of merit, z, is used, and typically is defined in its dimensionless form zT, which can be calculated through $zT = S^2 \sigma (\kappa_{ph} + \kappa_e)^{-1} T$, where S, σ, κ_{ph}, κ_e, and T depict Seebeck coefficient, electrical conductivity, lattice thermal conductivity, electronic thermal conductivity, and absolute temperature, respectively.[6]

Half-Heusler materials are quite well-known for their mechanical[7] and thermal[8] stability for medium temperature range applications up to 1000 K. For n-type materials, XNiSn (X = Ti, Zr, Hf) based compounds are among the most promising candidates, demonstrating a zT_{max} value above unity at high temperature ($T \geq 700$ K).[9,10] For p-type materials, Sn doped XCoSb (X = Ti, Zr, Hf) solid solutions exhibit high performance with a zT_{max} value of around unity at temperatures higher than 1000 K[11,12] with the exception of ~ 1.3 at 900 K for the $Ti_{0.5}Hf_{0.5}CoSn_{0.15}Sb_{0.85}$ material. It should be noted that the zT_{max} of ~ 1.3 was achieved using the experimental specific heat value which was lower than the Dulong-Petit approximation.[13] Among the p-type compounds, NbFeSb based half-Heusler materials have attracted substantial attention in recent years. NbFeSb follows the 18 electron rule (Nb ($5s^2 4d^3$), Fe ($4s^2 3d^6$), Sb ($5s^2 5p^3$)), thus depicting non-degenerate semiconducting behavior in an undoped state.[14] The undoped compound has a lattice parameter of ~ 5.95 Å,[15–17] and is stable at high temperature concerning the decomposition under exclusion of air, with little tolerance toward off-

stoichiometric variation. NbFeSb mainly shows an intrinsic *p*-type behavior with a fairly narrow indirect band gap of ~ 0.54 eV.[18,19] A previous study by Fu et al. showed that hole doping with Hf on the Nb site could simultaneously enhance the electrical conductivity and reduce the thermal conductivity resulting in a maximum figure of merit, zT_{max}, of ~ 1.5 at 1200 K for the $Nb_{0.88}Hf_{0.12}FeSb$ compound.[20] Furthermore, introducing Ta to Ti doped samples[21] led to lowering the thermal conductivity without significantly affecting the electrical properties, leading to a record high zT_{max} value of ~ 1.6 at 1200 K for the $(Nb_{0.6}Ta_{0.4})_{0.8}Ti_{0.2}FeSb$ (≡ $Nb_{0.48}Ta_{0.32}Ti_{0.2}FeSb$) sample. The positive effect of Ta substitution on Nb site in reducing the lattice thermal conductivity and maintaining the carrier mobility could partially be attributed to the lanthanide contraction effect.[22]

It is worth to mention that no "$NbFe_2Sb$" full-Heusler phase is detected in this system due to its low chemical stability.[23,24] Therefore, no full-Heusler/half-Heusler composite is expected to form here in case of excess iron. For the synthesis of NbFeSb based compounds, so far the typical arc melting[25] or levitation melting[21] process proceeded by a milling or annealing step were employed. Since all the melting techniques require high temperature (typically > 1900 K) and Sb possesses high vapor pressure at elevated temperatures, controlling the amount of Sb to compensate the loss can be challenging.

Although Ta showed a positive effect on the thermoelectric properties of Ti-doped NbFeSb samples, to the best of authors' knowledge, there is no report on the effect of Ta on Hf-doped samples. High energy ball milling of constituent elements proven to be a reliable synthesis method for high efficiency half-Heusler compounds such as ZrCoBi[26] and TaFeSb[27]. Therefore in this study, we utilize a facile synthesis route with direct high energy milling of the constituent elements followed by a sintering step to obtain high purity compacted half-Heusler samples. The

melting step is eliminated to prevent Sb loss. The effects of Ta substitution on microstructure and transport properties of the Hf-doped samples are examined.

2. Experimental section

The $Nb_{0.88-x}Hf_{0.12}Ta_xFeSb$ ($0 \leq x \leq 0.15$) samples were synthesized using Nb powder (99.9%, Evochem, 70-180 μm), Hf powder (99.6%, Alfa Aesar, -325 mesh), Ta powder (99.9%, ChemPur, <100 μm), Fe powder (99.998%, Alfa Aesar, -22 mesh), and Sb powder (99.999%, Alfa Aesar, -200 mesh). The elemental powders were mixed in the stoichiometric ratio, and the mixture was then ball milled for ~ 12 hours employing a high-energy SPEX Sample Prep 8000D Mixer Mill with stainless steel jars and balls. The mechanically milled powder was sintered in partial argon atmosphere at 1123 K for 20 minutes under a uniaxial pressure of ~ 64 MPa utilising a Direct-Current Sintering Press (Dr. Fritsch GmbH, DSP 510 SE). The pellets were passively cooled down, while the pressure was released during the cooling step to mitigate the strain and stress induced by the sintering process.

The electronic structures were computed utilizing the WIEN2k package applying the full-potential linearized augmented plane wave (FP-LAPW) method with the density functional theory (DFT).[28,29] The generalized gradient approximation (GGA) from a revised form of Perdew, Burke and Ernzerhof (PBE),[30] namely PBEsol,[31] was utilized for the exchange and correlation energies. The BoltzTraP code was used to determine the semiclassical transport parameters, which employs the Boltzmann transport theory with constant relaxation time approximation.[32] Spin-orbit coupling was included for the elements of period 6, namely Hf and Ta. Different supercells were created to enable calculations of the doped samples, and all lattice parameters were obtained via volume optimization. To investigate the effect of the Hf

concentration, we created models of the formula $Nb_3HfFe_4Sb_4$ ($Nb_{0.75}Hf_{0.25}FeSb$, space group $P\bar{4}3m$ with a = 6.007 Å) and $Nb_7HfFe_8Sb_8$ ($Nb_{0.875}Hf_{0.125}FeSb$, space group $P\bar{4}2m$ with a = 11.272 Å and c = 22.545 Å). The impact of a small substitution of Ta for Nb was investigated with the $Nb_6HfTaFe_8Sb_8$ model ($Nb_{0.75}Hf_{0.125}Ta_{0.125}FeSb$, space group $P\bar{4}2m$ with a = 11.230 Å and c = 22.545 Å). For the self-consistent calculations of the first cubic model, 35 independent k points were selected on a grid of 10 × 10 × 10 points spread out evenly throughout the Brillouin zone. For the two larger tetragonal cells, 63 independent k points were selected on a grid of 12 × 12 × 6 points. The energy convergence was set to be 10^{-4} Ry for the self-consistency.

A D8 Advanced Bruker X-ray diffractometer with Cu-$K_{\alpha 1}$ radiation was employed to verify the purity of the synthesized samples. X-ray diffraction patterns on the sintered pellets were shown in **Figure S1**. The electrical conductivity (σ) and Seebeck coefficient (S) measurements were performed on the sintered pellets (15.5 mm in diameter and ~ 3 mm in thickness). The measurements were carried out under helium atmosphere from 300 K to 800 K using an in-house developed facility (High Temperature Seebeck-Sigma Measurement Instrument) applying a four-probe method.[33,34]

Thermal diffusivity (α) measurement on the samples was performed in the same temperature range under Ar flow using the laser flash Netzsch LFA 427 apparatus. To obtain the thermal conductivity (κ), $\kappa = \alpha\ \rho\ c_p$, the measured diffusivity values were multiplied by the density (ρ) of the pellets, which measured through the Archimedes principle in ethanol, and the specific heat (c_p) of the compounds, as calculated employing the Dulong-Petit approximation. To analyze the microstructure of the compacted pellets, scanning electron microscopy (SEM) analysis was carried out on parts of pellets utilizing an ULTRA 55 electron microscope with a

Zeiss QBSE detector associated with an Oxford energy dispersive X-ray (EDX) device, EDAX PentaFETx3.

^{57}Fe conversion electron Mößbauer spectroscopy (CEMS) at perpendicular incidence of the gamma rays onto the sample pellet surface was performed by detection of conversion electrons. For the detection of the electrons, the samples were installed in a container with continuous helium gas flow mixed with 4% CH_4 to avoid ionization processes. For the measurement, a constant acceleration Mößbauer driving unit was employed with a ^{57}Co source embedded in a rhodium (Rh) matrix, while the velocity of the spectrometer was calibrated with an alpha-Fe foil reference sample at room temperature. Mößbauer spectra on powder samples were recorded in transmission geometry using a ^{57}Co gamma ray source mounted on a Mößbauer drive, operating in constant-acceleration mode. All the obtained experimental spectra were evaluated by a least-squares fitting routine using the Pi program package by Ulrich von Hörsten[35] with the spectra being referenced against alpha-Fe at room temperature. Low temperatures were achieved by the use of a liquid helium bath cryostat. For magnetic measurements, field and temperature dependent magnetization curves were recorded with the vibrating sample magnetometer (VSM) option of a Quantum Design PPMS DynaCool.

3. Results and Discussion

The density of states (DOS) were calculated for the models of $Nb_{0.875}Hf_{0.125}FeSb$, $Nb_{0.75}Hf_{0.125}Ta_{0.125}FeSb$, and $Nb_{0.75}Hf_{0.25}FeSb$. Replacing Nb with Hf removes one valence electron per replaced atom, making these materials *p*-doped semiconductors, i.e., the Fermi level (E_F) falls slightly below the top of the valence band in each case (**Figure 1**). Thus, the model

with the highest Hf content (0.25 per formula unit, **Figure 1**c) exhibits the most unfilled states and hence highest *p*-type charge carrier concentration. On the other hand, replacing Nb with isovalent Ta has almost no impact on the shape of the valence band at E_F (**Figure 1**a vs. **Figure 1**b). This is due to the facts that Nb and Ta have very similar electronic properties, and that the valence band is dominated by Fe-*d* and Sb-*p* states, with only minor contributions from X = Nb, Hf, and Ta because of covalent mixing via the X–Fe and X–Sb interactions, as also pointed out before by others.[17]

Figure 1 here

The electrical transport properties of all samples were measured in at least one heating and cooling cycle to assure the stability and reproducibility of the presented data. The electrical conductivity of all samples decreases with increasing temperature (with a trend of ~ $T^{1.5}$) mainly due to charge carrier scattering by acoustic phonons (**Figure 2**). A reduction in electrical conductivity is observed by introducing Ta to the system (from σ ~ 5100 $\Omega^{-1}cm^{-1}$ for the Ta-free sample to ~ 3900 $\Omega^{-1}cm^{-1}$ at ~ 326 K for the sample with 5 at.-% Ta on Nb site), which is slightly stronger than the one observed in $(Nb_{1-x}Ta_x)_{0.8}Ti_{0.2}FeSb$ samples (from ~ 6600 $\Omega^{-1}cm^{-1}$ to ~ 5500 $\Omega^{-1}cm^{-1}$ at ~ 300 K with x varying from 0 to 0.4).[21] To be sure about the validity of the results the second $Nb_{0.83}Hf_{0.12}Ta_{0.05}FeSb$ sample was pressed and measured applying the same condition and the obtained results were within the error range of the measurement (**Figure S2**). Considering the isovalent nature of Nb and Ta as well as their similar atomic sizes and chemical properties, the induced electric potential fluctuation by Ta is expected to be negligible.

Since the carrier concentration should remain the same (same Hf content), ideally, unless τ or the mobility changes, the electrical conductivity would remain the same, as also seen via BoltzTrap calculation: the calculated σ/τ curves of the $Nb_{0.875}Hf_{0.125}FeSb$ and $Nb_{0.75}Hf_{0.125}Ta_{0.125}FeSb$ models are virtually identical (**Figure 2**b). Moreover, τ is not expected to change with Nb and Ta having virtually the same sizes (~ 146 pm). It should be noted that we are plotting σ/τ against $\mu - E_F(0\ K)$, because the 0 K Fermi energies E_F of these materials are different despite having the same number of valence electrons.

Figure 2 here

To better understand the observed decay in electrical conductivity, the microstructures of the samples were studied using SEM/EDX. Although high homogeneity was observed on the SEM mapping of the samples on larger scale, e.g., in case of $Nb_{0.78}Hf_{0.12}Ta_{0.1}FeSb$ at a scale of ~ 25 μm (**Figure S3**), further line scan investigations revealed the existence of a Hf-rich half-Heusler phase in $Nb_{0.88}Hf_{0.12}FeSb$ sample (**Figure 3**a) as well as most likely binary hafnium antimonides at the grain boundaries in case of Ta containing samples such as $Nb_{0.83}Hf_{0.12}Ta_{0.05}FeSb$ and $Nb_{0.73}Hf_{0.12}Ta_{0.15}FeSb$ (**Figure 3**b and 3c). Specifically, the region with approximately 45 at.-% Hf and 55 at.-% Sb could be a mixture of metallic $HfSb_2$ and HfSb (noting that Hf_5Sb_9 is a high-temperature phase that should decompose below 1000 K).[36,37] While neither of these compounds was identified via X-ray powder diffraction because of their low concentrations, the microstructure studies reveal that the more Ta-rich samples are less homogenous. It should be noted that the binary hafnium antimonide phases are metallic.[38]

Figure 3 here

Simultaneously losing the dopant Hf, together with gaining metallic hafnium antimonides at the grain boundaries, could compensate the charge carrier concentration loss for the samples containing higher Ta content. These microstructure phases can not only impact the carrier mobility but also act as carrier donors and scattering centers depending on their sizes (e.g., as was observed in nano-inclusions), which can have significant contributions to materials´ transport properties such as in $Nb_{0.83}Hf_{0.12}Ta_{0.05}FeSb$.

The Seebeck coefficient of all samples is displayed in **Figure 4**a; except for the $Nb_{0.83}Hf_{0.12}Ta_{0.05}FeSb$ sample, they all exhibit a similar Seebeck value of ~ 75 μV K^{-1} at 300 K, which gradually increases with elevated temperature reaching ~ 172 μV K^{-1} at 800 K. The existence of metallic (e.g., full Heusler) phases, depending on their size and concentration, demonstrated a positive impact on Seebeck coefficient of $Ti_{0.1}Zr_{0.9}NiSn$[39] and $Zr_{0.25}Hf_{0.75}NiSn$[40] half-Heusler based materials. In our case however, considering the low electrical conductivity of $Nb_{0.83}Hf_{0.12}Ta_{0.05}FeSb$ compared to the other compositions, the loss of Hf as dopant which caused carrier concentration fluctuation could also be responsible for the obtained large Seebeck values. The Boltzmann transport calculations reveal that introducing Ta should have insignificant effects on the Seebeck coefficient (**Figure 4**b). Specifically, both calculated models with 12.5 at.-% Hf on the *X* sites, $Nb_{0.875}Hf_{0.125}FeSb$ and $Nb_{0.75}Hf_{0.125}Ta_{0.125}FeSb$, exhibit ~ 60 μV K^{-1} at 300 K at E_F, while the one with 25 at.-% Hf, i.e., formally twice as many charge carriers, has only ~ 45 μV K^{-1} at 300 K at E_F.

Figure 4 here

The temperature dependent thermal conductivity values of all samples are shown in **Figure 5**a. All the Ta containing samples demonstrate consistently lower (by 10% - 13%) thermal conductivity in the whole investigated temperature range, varying from ~ 7.0 W $m^{-1}K^{-1}$ at 350 K to ~ 4.5 W $m^{-1}K^{-1}$ at 800 K. To unravel the effect of Ta on the lattice thermal conductivity, the lattice part of thermal conductivity, κ_L, was deducted from the total thermal conductivity, κ, by subtracting the electronic contribution (**Figure 5**a), κ_e, which was calculated utilizing the Wiedemann-Franz law, $\kappa_e = L \cdot \sigma \cdot T$. To obtain κ_e, the Lorenz number, L, was calculated at various temperatures through employing the equation $L = 1.5 + \exp\left[-\frac{|S|}{116}\right]$,[41] where S is in μV K^{-1} and L in 10^{-8} V^2K^{-2}. The accuracy of obtained L values is within 5% for single parabolic band (SPB)/acoustic phonon scattering and within 20% for more complex scattering mechanisms, such as non-parabolic Kane bands, and multiple bands. The lattice thermal conductivity (**Figure 5**b) decreases with increasing the Ta content, reaching a minimum value of ~ 3.6 W $m^{-1}K^{-1}$ at 350 K, which is ~ 28% lower than that of the sample without Ta. This reduction in thermal conductivity is partially attributed to the large point defect scattering caused by Ta substitution, which increases mass fluctuation. The calculation of the disorder parameter Γ (**Figure 5**c) shows that total disorder Γ_{total} increases with increasing Ta content indicating a stronger point defect scattering at higher Ta content. Since the atomic radii of Ta and Nb are quite similar, there is no significant additional strain field fluctuation Γ_s induced by Ta substitution; thus the Γ_s remains unchanged for all the samples. Consequently, the increase in

Γ_{total} is mainly ascribed to the intense mass fluctuation leading to the increase in mass disorder Γ_m.[42]

The strong point defect scattering at higher temperature is consistent with the linear dependence of κ_L versus $T^{-0.5}$ (**Figure S4**). Typically, the phonons can be scattered via different mechanisms such as point defects, Umklapp process (phonon-phonon interaction), boundary scattering, and electron-phonon interactions. To estimate the contribution of each mechanism, the phonon relaxation time is calculated at different frequencies (**Figure 5**d). The calculation details are available in the supplementary information, and 400 K is chosen for the temperature since all the vibration modes have been excited considering the Debye frequency as the maximum phonon frequency.[43] As can be seen, phonons with higher frequencies are mainly targeted by Umklapp and point defect scattering, whereas electron-phonon and boundary scattering becomes more dominant at low frequencies, which is typically the predicted case.[44,45] It is worth to mention that for the calculation of boundary scattering, an average value of 1.5 μm was used for the grain size based on the SEM and particle size analysis, whereas in reality, the grain sizes vary within the sample; thus the calculated value here is overestimated due to the presence of larger grains. The lattice thermal conductivity values are still substantially larger than the theoretical minimum value, κ_{min}, (~0.9 W $m^{-1}K^{-1}$) obtained from Cahill's model[46] indicating the possibility of further reduction in thermal conductivity to improve the efficiency for these compounds.

Figure 5 here

To shed more light on the electronic behavior of $Nb_{0.83}Hf_{0.12}Ta_{0.05}FeSb$ sample compared with the non-substituted sample, conversion electron Mößbauer spectroscopy was performed on the $Nb_{0.88}Hf_{0.12}FeSb$ and $Nb_{0.83}Hf_{0.12}Ta_{0.05}FeSb$ pellets at room temperature (**Figure 6**), each showing a single peak with rather minute differences between the two samples, clearly indicating that there is no magnetic ordering present at room temperature. This behavior is indicative of Fe atoms occupying exclusively one site as it has also been found in the similar half-Heusler system of VFeSb.[47] The only deviation from a pure singlet state was a minor shoulder (marked by an arrow), which can be somewhat alleviated using a doublet fit function with a very small quadrupole splitting (0.16 mm s^{-1} - 0.20 mm s^{-1}). This could be a general indicator for the presence of a small number of Fe atoms on different lattice sites. The occupation of Fe next neighbor sites with different elements could give rise to a small electric field gradient at the Fe nucleus position, which is responsible for this minor doublet splitting, and not visible to the naked eye due to it being smaller than the absorption line width. A slight increase in linewidth can also be caused by minor structural disorders. However, both samples showed nearly identical behavior, indicating that the Ta substitution does not significantly alter the fundamental magnetic properties. To further investigate these properties, spectra were recorded on sample powder, obtained by crushing a small piece of the original pellet. These measurements were performed in transmission geometry at 4.3 K (below common Curie or Néel temperature) to ensure that any potentially magnetic phase is in its ordered state. However, the spectra revealed only single peaks, not pointing to any kind of magnetic ordering of the Fe ions. At room temperature, a satisfactory fit could be obtained by a doublet with a very small quadrupole splitting in the range of 0.14 mm s^{-1} - 0.19 mm s^{-1}.

Figure 6 here

Additionally, a standard magnetometry characterization on the same powders was performed (**Figure S5**). Although the samples seem to show mostly paramagnetic behavior in the $M(H)$ curves, there is a very small spontaneous magnetization clearly visible at 300 K (**Figure S5**a). When comparing these findings to the Mößbauer results, it is obvious that this signal is not coming from the dominant Fe-bearing phase of the sample and must thus have different origins. It is possible that a minor parasitic Fe-bearing phase is present, in the range of less than 5 at.-%, which would still be within the background noise of the otherwise strong singlet spectra. The result of the temperature dependent $M(T)$ measurement (**Figure S5**b) also showed a clear phase transition at ~ 150 K in the Ta doped sample compared to the non-doped one, which might be due to extrinsic defects induced by Ta into the system. No corresponding change in spectral structure was visible when comparing room and low temperature Mößbauer spectra, supporting the notion that the observed magnetic properties are not dictated by the dominant Fe-bearing phase of the half-Heusler. This could also be indicative for the formation of a minute parasitic phase, possibly a different Heusler phase, as the magnetization shows a spontaneous but very small drop upon exceeding 150 K, possibly indicating a first-order phase transition.

Figure 7 shows the temperature dependence of the dimensionless figure of merit, zT, for all samples up to 800 K. All samples demonstrate a quite similar figure of merit of ~ 0.15 at 300 K which enhances with increasing temperature to around 0.75 at 800 K, and is comparable with the $Nb_{0.608}Ta_{0.192}Ti_{0.2}FeSb$ sample reported by Yu et al. which showed zT of ~ 1.5 at 1200 K.[21] Consequently, higher zT values are expected at higher temperature in the cases presented here, as

the values continue to increase during the whole measurement temperature range (300 K to 800 K). To further enhance the figure of merit, other approaches such as full-Heusler inclusions (with different compounds such as $NbFe_2Al$ due to the instability of $NbFe_2Sb$) or hierarchical structural engineering could be beneficial to affect the thermal conductivity without impacting the electronic transport properties.

Figure 7 here

4. Conclusions

In summary, we present a thorough study on microstructure, electronic and thermal transport properties as well as some preliminary results on magnetic properties of the $Nb_{0.88-x}Hf_{0.12}Ta_xFeSb$ half-Heusler thermoelectric materials. All the samples were successfully synthesized employing the facile high energy ball milling synthesis technique proceeded by direct current sintering. All samples exhibited reproducible and thermally stable properties within the measured temperature range. Although introducing Ta decreased the electrical conductivity, all samples demonstrated the degenerate semiconducting character with the electrical conductivity higher than 3500 $\Omega^{-1}cm^{-1}$ at 326 K. Apart from the $Nb_{0.83}Hf_{0.12}Ta_{0.05}FeSb$ sample with the maximum Seebeck coefficient of 184 $\mu V\ K^{-1}$ at 800 K, all other compositions exhibit similar Seebeck values of around 172 $\mu V\ K^{-1}$ at the same temperature. Microstructure study via SEM/EDX showed that the detrimental impact of Ta on the electronic transport properties could be attributed to the formation of Hf-rich and metallic hafnium antimonide

phases. A clear trend on the reduction of lattice thermal conductivity was observed for the Ta-containing samples proving the beneficial effects of Ta substitution. The lattice thermal conductivity of all samples decreased with increasing Ta content mainly due to the mass fluctuation disorder coming from the substitution of heavy Ta atoms, leading to ~ 28% reduction in κ_L at 350 K for the material containing 15 at.-% Ta on Nb sites. The $Nb_{0.83}Hf_{0.12}Ta_{0.05}FeSb$ sample showed a magnetic phase transition at ~ 150 K, which might be due to extrinsic defects induced by Ta substitution. The magnetic properties were not strongly altered by the Ta substitutions, with the dominant Fe-bearing Heusler phase remaining paramagnetic down to low temperatures, while macroscopic magnetometry measurements revealed a small spontaneous magnetization, possibly indicating a very minute parasitic phase observed in the microstructure. All in all, the dimensionless figure of merit, zT, is quite similar for all samples reaching a value of ~ 0.75 at 800 K due to the compensating effect of Ta substitution on the thermal and electrical transport properties. This efficiency is analogous to that of $Nb_{0.608}Ta_{0.192}Ti_{0.2}FeSb$ sample reported by Yu et al.[21] that reached ~ 1.5 at 1200 K.

ASSOCIATED CONTENT

Supporting Information. X-ray diffraction patterns of pressed $Nb_{0.88-x}Hf_{0.12}Ta_xFeSb$ ($0 \leq x \leq 0.15$) samples. Electrical conductivity comparison between two $Nb_{0.83}Hf_{0.12}Ta_{0.05}FeSb$ samples. SEM mapping of the $Nb_{0.78}Hf_{0.12}Ta_{0.1}FeSb$ sample. The lattice thermal conductivity values of the $Nb_{0.88-x}Hf_{0.12}Ta_xFeSb$ ($0 \leq x \leq 0.15$) samples versus $T^{-0.5}$. Magnetometry characterization of $Nb_{0.88}Hf_{0.12}FeSb$ and $Nb_{0.83}Hf_{0.12}Ta_{0.05}FeSb$ powders (**a**) $M(H)$ at 5 K and 300 K, (**b**) $M(T)$ at 0.1 T from 5 K to 300 K. Phonon relaxation time calculation procedure and the parameters used for calculation.

Corresponding Author

*Email: nfarahi@uwaterloo.ca.

Author Contributions

The manuscript was written through contributions of all authors. All authors have given approval to the final version of the manuscript.

ACKNOWLEDGMENT

The authors would like to kindly acknowledge the support from the endorsement from the DLR Executive Board Member for Space Research and Technology and the financial support from the Young Research Group Leader Program. We would also like to thank P. Blaschkewitz and P. Ziolkowski for their support with the thermoelectric measurements. N.F. would like to thank the German Academic Exchange Service (DAAD) for financial support from the DLR-DAAD Fellowship Programme, project No. 248. The work at the University of Waterloo was supported by an NSERC Discovery Grant (RGPIN-2015-04584). Also, one of the authors (JdB) is partially funded by the Deutsche Forschungsgemeinschaft (DFG, German Research Foundation)-project number 396709363. The authors would also like to thank the DFG for funding via the CRC 1242 (project A05), CRC/TRR 247 (project B2), SPP1681 (WE2623/7-3) and WE2623/14-1.

REFERENCES

(1) Anatychuk, L. I.; Rozver, Y. Y.; Velichuk, D. D. Thermoelectric Generator for a Stationary Diesel Plant. *J. Electron. Mater.* **2011**, *40* (5), 1206–1208. https://doi.org/10.1007/s11664-011-1600-6.

(2) Yang, J.; Stabler, F. R. Automotive Applications of Thermoelectric Materials. *J. Electron. Mater.* **2009**, *38* (7), 1245–1251. https://doi.org/10.1007/s11664-009-0680-z.

(3) Farahi, N.; Stiewe, C.; Truong, D. Y. N.; de Boor, J.; Müller, E. High Efficiency Mg2(Si,Sn)-Based Thermoelectric Materials: Scale-up Synthesis, Functional Homogeneity, and Thermal Stability. *RSC Adv.* **2019**, *9* (40), 23021–23028. https://doi.org/10.1039/C9RA04800F.

(4) Farahi, N.; Prabhudev, S.; Botton, G. A.; Salvador, J. R.; Kleinke, H. Nano-and Microstructure Engineering: An Effective Method for Creating High Efficiency Magnesium Silicide Based Thermoelectrics. *ACS Appl. Mater. Interfaces* **2016**, *8* (50), 34431–34437.

(5) Sankhla, A.; Patil, A.; Kamila, H.; Yasseri, M.; Farahi, N.; Mueller, E.; de Boor, J. Mechanical Alloying of Optimized Mg2 (Si, Sn) Solid Solutions: Understanding Phase Evolution and Tuning Synthesis Parameters for Thermoelectric Applications. *ACS Appl. Energy Mater.* **2018**, *1* (2), 531–542.

(6) Ioffe, A. F. *Physics of Semiconductors*; Academic Press: New York City, NY, 1960.

(7) Rogl, G.; Grytsiv, A.; Gürth, M.; Tavassoli, A.; Ebner, C.; Wünschek, A.; Puchegger, S.; Soprunyuk, V.; Schranz, W.; Bauer, E.; Müller, H.; Zehetbauer, M.; Rogl, P. Mechanical Properties of Half-Heusler Alloys. *Acta Mater.* **2016**, *107*, 178–195. https://doi.org/10.1016/j.actamat.2016.01.031.

(8) Rausch, E.; Balke, B.; Ouardi, S.; Felser, C. Long-Term Stability of (Ti/Zr/Hf)$CoSb_{1-x}Sn_x$ Thermoelectric p-Type Half-Heusler Compounds Upon Thermal Cycling. *Energy Technol.* **2015**, *3* (12), 1217–1224. https://doi.org/10.1002/ente.201500183.

(9) Chen, L.; Liu, Y.; He, J.; Tritt, T. M.; Poon, S. J. High Thermoelectric Figure of Merit by

Resonant Dopant in Half-Heusler Alloys. *AIP Adv.* **2017**, *7* (6). https://doi.org/10.1063/1.4986760.

(10) Rogl, G.; Sauerschnig, P.; Rykavets, Z.; Romaka, V. V.; Heinrich, P.; Hinterleitner, B.; Grytsiv, A.; Bauer, E.; Rogl, P. (V,Nb)-Doped Half Heusler Alloys Based on {Ti,Zr,Hf}NiSn with High ZT. *Acta Mater.* **2017**, *131*, 336–348. https://doi.org/10.1016/j.actamat.2017.03.071.

(11) Yan, X.; Liu, W.; Chen, S.; Wang, H.; Zhang, Q.; Chen, G.; Ren, Z. Thermoelectric Property Study of Nanostructured P-Type Half-Heuslers (Hf, Zr, Ti)$CoSb_{0.8}$ $Sn_{0.2}$. *Adv. Energy Mater.* **2013**, *3* (9), 1195–1200. https://doi.org/10.1002/aenm.201200973.

(12) Yan, X.; Liu, W.; Wang, H.; Chen, S.; Shiomi, J.; Esfarjani, K.; Wang, H.; Wang, D.; Chen, G.; Ren, Z. Stronger Phonon Scattering by Larger Differences in Atomic Mass and Size in P-Type Half-Heuslers $Hf_{1-x}Ti_xCoSb_{0.8}Sn_{0.2}$. *Energy Environ. Sci.* **2012**, *5* (6), 7543–7548. https://doi.org/10.1039/c2ee21554c.

(13) Rausch, E.; Castegnaro, M. V.; Bernardi, F.; Martins Alves, M. C.; Morais, J.; Balke, B. Short and Long Range Order of Half-Heusler Phases in (Ti,Zr,Hf)CoSb Thermoelectric Compounds. *Acta Mater.* **2016**, *115*, 308–313. https://doi.org/10.1016/j.actamat.2016.05.041.

(14) He, R.; Kraemer, D.; Mao, J.; Zeng, L.; Jie, Q.; Lan, Y.; Li, C.; Shuai, J.; Kim, H. S.; Liu, Y.; Broido, D.; Chu, C.-W.; Chen, G.; Ren, Z. Achieving High Power Factor and Output Power Density in P-Type Half-Heuslers $Nb_{1-x}Ti_xFeSb$. *Proc. Natl. Acad. Sci.* **2016**, *113* (48), 13576–13581. https://doi.org/10.1073/pnas.1617663113.

(15) Silpawilawan, W.; Kurosaki, K.; Ohishi, Y.; Muta, H.; Yamanaka, S. FeNbSb P-Type Half-Heusler Compound: Beneficial Thermomechanical Properties and High-Temperature Stability for Thermoelectrics. *J. Mater. Chem. C* **2017**, *5* (27), 6677–6681. https://doi.org/10.1039/c7tc01570d.

(16) Fu, C.; Zhu, T.; Liu, Y.; Xie, H.; Zhao, X. Band Engineering of High Performance P-Type FeNbSb Based Half-Heusler Thermoelectric Materials for Figure of Merit ZT > 1. *Energy Environ. Sci.* **2015**, *8*, 216–220. https://doi.org/10.1039/c4ee03042g.

(17) Fang, T.; Zheng, S.; Chen, H.; Cheng, H.; Wang, L.; Zhang, P. Electronic Structure and Thermoelectric Properties of P-Type Half-Heusler Compound NbFeSb: A First-Principles Study. *RSC Adv.* **2016**, *6* (13), 10507–10512. https://doi.org/10.1039/c5ra23091h.

(18) Page, A.; Poudeu, P. F. P.; Uher, C. A First-Principles Approach to Half-Heusler Thermoelectrics: Accelerated Prediction and Understanding of Material Properties. *J. Mater.* **2016**, *2* (2), 104–113. https://doi.org/10.1016/j.jmat.2016.04.006.

(19) Bhattacharya, S.; Madsen, G. K. H. A Novel P-Type Half-Heusler from High-Throughput Transport and Defect Calculations. *J. Mater. Chem. C* **2016**, *4* (47), 11261–11268. https://doi.org/10.1039/c6tc04259g.

(20) Fu, C.; Bai, S.; Liu, Y.; Tang, Y.; Chen, L.; Zhao, X.; Zhu, T. Realizing High Figure of Merit in Heavy-Band p-Type Half-Heusler Thermoelectric Materials. *Nat. Commun.* **2015**, *6*, 1–7. https://doi.org/10.1038/ncomms9144.

(21) Yu, J.; Fu, C.; Liu, Y.; Xia, K.; Aydemir, U.; Chasapis, T. C.; Snyder, G. J.; Zhao, X.; Zhu, T. Unique Role of Refractory Ta Alloying in Enhancing the Figure of Merit of

NbFeSb Thermoelectric Materials. *Adv. Energy Mater.* **2018**, *8* (1), 1701313. https://doi.org/10.1002/aenm.201701313.

(22) Liu, Y.; Fu, C.; Xia, K.; Yu, J.; Zhao, X.; Pan, H.; Felser, C.; Zhu, T. Lanthanide Contraction as a Design Factor for High-Performance Half-Heusler Thermoelectric Materials. *Adv. Mater.* **2018**, *30* (32), 1800881. https://doi.org/10.1002/adma.201800881.

(23) Melnyk, G.; Leithe-Jasper, A.; Rogl, P.; Skolozdra, R. The Antimony-Iron-Niobium (Sb-Fe-Nb) System. *J. Phase Equilibria* **1999**, *20* (2), 113–118. https://doi.org/10.1007/s11669-999-0009-x.

(24) Lomnitska, Y. F. Interaction of Niobium and Iron with Stibium. *Powder Metall. Met. Ceram.* **2008**, *47* (7–8), 447–450. https://doi.org/10.1007/s11106-008-9040-4.

(25) Young, D. P.; Khalifah, P.; Cava, R. J.; Ramirez, A. P. Thermoelectric Properties of Pure and Doped FeMSb (M=V,Nb). *J. Appl. Phys.* **2000**, *87* (1), 317–321. https://doi.org/10.1063/1.371863.

(26) Zhu, H.; He, R.; Mao, J.; Zhu, Q.; Li, C.; Sun, J.; Ren, W.; Wang, Y.; Liu, Z.; Tang, Z.; Sotnikov, A.; Wang, Z.; Broido, D.; Singh, D. J.; Chen, G.; Nielsch, K.; Ren, Z. Discovery of ZrCoBi Based Half Heuslers with High Thermoelectric Conversion Efficiency. *Nat. Commun.* **2018**, *9* (1), 1–9. https://doi.org/10.1038/s41467-018-04958-3.

(27) Zhu, H.; Mao, J.; Li, Y.; Sun, J.; Wang, Y.; Zhu, Q.; Li, G.; Song, Q.; Zhou, J.; Fu, Y.; He, R.; Tong, T.; Liu, Z.; Ren, W.; You, L. Wang, Z.; Luo, J.; Sotnikov, A.; Bao, J.; Nielsch, K.; Chen, G.; Singh, D. J.; Ren, Z. Discovery of TaFeSb-Based Half-Heuslers with High Thermoelectric Performance. *Nat. Commun.* **2019**, *10* (1), 270.

https://doi.org/10.1038/s41467-018-08223-5.

(28) Blaha, P.; Schwarz, K.; Madsen, G. K. H.; Kvasnicka, D.; Luitz, J. *WIEN2k, An Augmented Plane Wave plus Local Orbitals Program for Calculating Crystal Properties*; Schwarz, K., Ed.; Techn. Universität Wien, Austria, 2001.

(29) Schwarz, K. DFT Calculations of Solids with LAPW and WIEN2k. *J. Solid State Chem.* **2003**, *176* (2), 319–328. https://doi.org/10.1016/S0022-4596(03)00213-5.

(30) Perdew, J. P.; Burke, K.; Ernzerhof, M. Generalized Gradient Approximation Made Simple. *Phys. Rev. Lett.* **1996**, *77* (18), 3865–3868. https://doi.org/10.1103/PhysRevLett.77.3865.

(31) Perdew, J. P.; Ruzsinszky, A.; Csonka, G. I.; Vydrov, O. A.; Scuseria, G. E.; Constantin, L. A.; Zhou, X.; Burke, K. Restoring the Density-Gradient Expansion for Exchange in Solids and Surfaces. *Phys. Rev. Lett.* **2008**, *100* (13), 136406/1-4. https://doi.org/10.1103/PhysRevLett.100.136406.

(32) Madsen, G. K. H.; Singh, D. J. BoltzTraP. A Code for Calculating Band-Structure Dependent Quantities. *Comput. Phys. Commun.* **2006**, *175* (1), 67–71. https://doi.org/10.1016/j.cpc.2006.03.007.

(33) de Boor, J.; Stiewe, C.; Ziolkowski, P.; Dasgupta, T.; Karpinski, G.; Lenz, E.; Edler, F.; Mueller, E. High-Temperature Measurement of Seebeck Coefficient and Electrical Conductivity. *J. Electron. Mater.* **2013**, *42* (7), 1711–1718. https://doi.org/10.1007/s11664-012-2404-z.

(34) de Boor, J.; Müller, E. Data Analysis for Seebeck Coefficient Measurements. *Rev. Sci. Instrum.* **2013**, *84* (6), 65102. https://doi.org/10.1063/1.4807697.

(35) von Hörsten U 2015 'Pi' Program Package https://www.uni-due.de/~hm236ap/hoersten/home.html.

(36) Assoud, A.; Kleinke, K. M.; Soheilnia, N.; Kleinke, H. T-Shaped Nets of Sb Atoms in the Binary Antimonide Hf5Sb9. *Angew. Chem. Int. Ed.* **2004**, *43*, 5260–5262.

(37) Xu, J.; Kleinke, K. M.; Kleinke, H. Electronic Structure and Physical Properties of Hf_5Sb_9 Containing a Unique T Net of Sb Atoms. *Zeitschrift fur Anorg. und Allg. Chemie* **2008**, *634* (12–13), 2367–2372. https://doi.org/10.1002/zaac.200800288.

(38) Kleinke, H.; Felser, C. New Binary Antimonide Hf5Sb3. *J. Alloys Compd.* **1999**, *291* (1–2), 73–79. https://doi.org/10.1016/S0925-8388(99)00282-0.

(39) Liu, Y.; Sahoo, P.; Makongo, J. P. A.; Zhou, X.; Kim, S.-J.; Chi, H.; Uher, C.; Pan, X.; Poudeu, P. F. P. Large Enhancements of Thermopower and Carrier Mobility in Quantum Dot Engineered Bulk Semiconductors. *J. Am. Chem. Soc.* **2013**, *135* (20), 7486–7495. https://doi.org/10.1021/ja311059m.

(40) Makongo, J. P. A.; Misra, D. K.; Zhou, X.; Pant, A.; Shabetai, M. R.; Su, X.; Uher, C.; Stokes, K. L.; Poudeu, P. F. P. Simultaneous Large Enhancements in Thermopower and Electrical Conductivity of Bulk Nanostructured Half-Heusler Alloys. *J. Am. Chem. Soc.* **2011**, *133* (46), 18843–18852. https://doi.org/10.1021/ja206491j.

(41) Kim, H.-S.; Gibbs, Z. M.; Tang, Y.; Wang, H.; Snyder, G. J. Characterization of Lorenz

Number with Seebeck Coefficient Measurement. *APL Mater.* **2015**, *3* (4), 41506. https://doi.org/10.1063/1.4908244.

(42) Abeles, B. Lattice Thermal Conductivity of Disordered Semiconductor Alloys at High Temperatures. *Phys. Rev.* **1963**, *131* (5), 1906–1911. https://doi.org/10.1103/PhysRev.131.1906.

(43) Xie, H.; Wang, H.; Pei, Y.; Fu, C.; Liu, X.; Snyder, G. J.; Zhao, X.; Zhu, T. Beneficial Contribution of Alloy Disorder to Electron and Phonon Transport in Half-Heusler Thermoelectric Materials. *Adv. Funct. Mater.* **2013**, *23* (41), 5123–5130. https://doi.org/10.1002/adfm.201300663.

(44) Bhandari, C. M.; Rowe, D. M. *Thermal Conduction in Semiconductors*; John Wiley & Sons, Ltd: New York, 1988. https://doi.org/10.1002/piuz.19890200506.

(45) Tritt, T. M. *Thermal Conductivity*; Physics of Solids and Liquids; Springer: New York City, NY, 2004. https://doi.org/10.1007/b136496.

(46) Cahill, D. G.; Watson, S. K.; Pohl, R. O. Lower Limit to the Thermal Conductivity of Disordered Crystals. *Phys. Rev. B* **1992**, *46* (10), 6131–6140. https://doi.org/10.1103/PhysRevB.46.6131.

(47) Jodin, L.; Tobola, J.; Pecheur, P.; Scherrer, H.; Kaprzyk, S. Effect of Substitutions and Defects in Half-Heusler FeVSb Studied by Electron Transport Measurements and KKR-CPA Electronic Structure Calculations. *Phys. Rev. B - Condens. Matter Mater. Phys.* **2004**, *70* (18), 1–11. https://doi.org/10.1103/PhysRevB.70.184207.

(48) Yang, J.; Meisner, G. P.; Chen, L. Strain Field Fluctuation Effects on Lattice Thermal Conductivity of ZrNiSn-Based Thermoelectric Compounds. *Appl. Phys. Lett.* **2004**, *85* (7), 1140–1142. https://doi.org/10.1063/1.1783022.

Figure captions

Figure 1. Density of states of (**a**) the $Nb_{0.875}Hf_{0.125}FeSb$ model; (**b**) the $Nb_{0.75}Hf_{0.125}Ta_{0.125}FeSb$ model; and (**c**) the $Nb_{0.75}Hf_{0.25}FeSb$ model.

Figure 2. (**a**) Electrical conductivity of the $Nb_{0.88-x}Hf_{0.12}Ta_xFeSb$ ($0 \leq x \leq 0.15$) samples; and (**b**) calculated electrical conductivity over relaxation time (τ) against chemical potential at 300 K.

Figure 3. SEM images and line scan analyses of Hf-rich regions and hafnium antimonide compounds at the grain boundaries observed in (**a**) $Nb_{0.88}Hf_{0.12}FeSb$, (**b**) $Nb_{0.83}Hf_{0.12}Ta_{0.05}FeSb$, and (**c**) $Nb_{0.73}Hf_{0.12}Ta_{0.15}FeSb$ samples.

Figure 4. (**a**) Seebeck coefficient of the $Nb_{0.88-x}Hf_{0.12}Ta_xFeSb$ ($0 \leq x \leq 0.15$) samples; and (**b**) calculated Seebeck coefficient against chemical potential at 300 K.

Figure 5. (**a**) Thermal conductivity (solid symbols), electronic part of thermal conductivity (open symbols); (**b**) lattice thermal conductivity of the $Nb_{0.88-x}Hf_{0.12}Ta_xFeSb$ ($0 \leq x \leq 0.15$) samples; (**c**) the calculated disorder parameter Γ for $Nb_{0.88-x}Hf_{0.12}Ta_xFeSb$ ($0 \leq x \leq 0.15$) samples, where Γ_M and Γ_s are mass and strain field fluctuations, respectively, and Γ_{total} is their sum ($\Gamma_{total} = \Gamma_M + \Gamma_s$);[48] and (**d**) phonon relaxation time against frequency at 400 K for $Nb_{0.73}Hf_{0.12}Ta_{0.15}FeSb$ sample.

Figure 6. Mößbauer spectroscopy results for the $Nb_{0.88}Hf_{0.12}FeSb$ (blue) and $Nb_{0.83}Hf_{0.12}Ta_{0.05}FeSb$ (red) samples at room temperature (left) and 4.3 K (right), reproduced via a doublet of absorption lines, appearing as a single line due to the small quadrupole splitting.

Figure 7. Temperature dependent dimensionless figure of merit of the $Nb_{0.88-x}Hf_{0.12}Ta_xFeSb$ ($0 \leq x \leq 0.15$) samples, compared with the $Nb_{0.608}Ta_{0.192}Ti_{0.2}FeSb$ sample (star symbol) reported by Yu et al.[21]

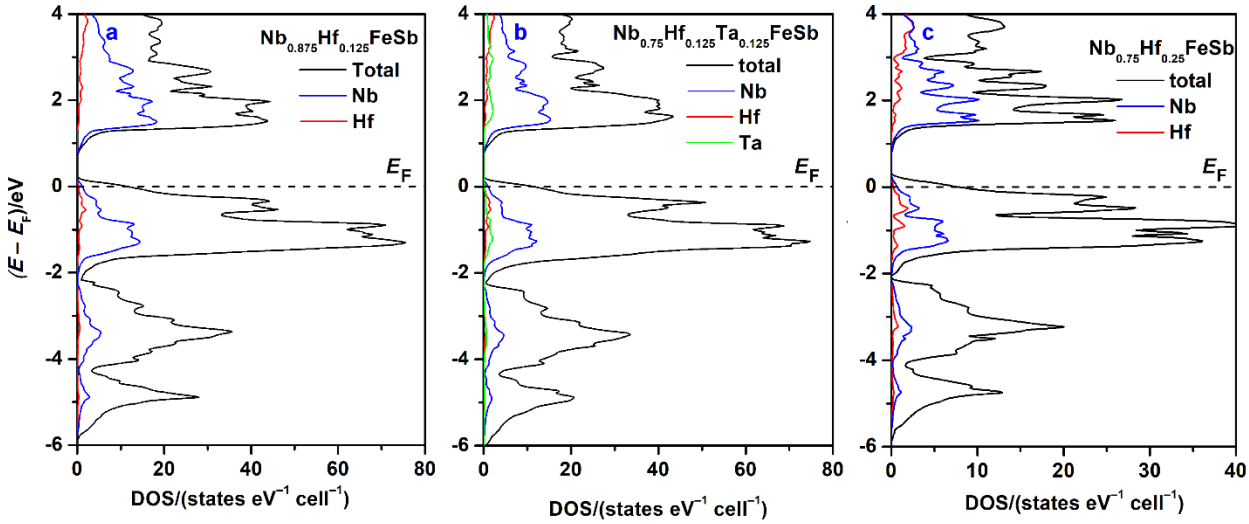

Figure 1. Density of states of (**a**) the $Nb_{0.875}Hf_{0.125}FeSb$ model; (**b**) the $Nb_{0.75}Hf_{0.125}Ta_{0.125}FeSb$ model; and (**c**) the $Nb_{0.75}Hf_{0.25}FeSb$ model.

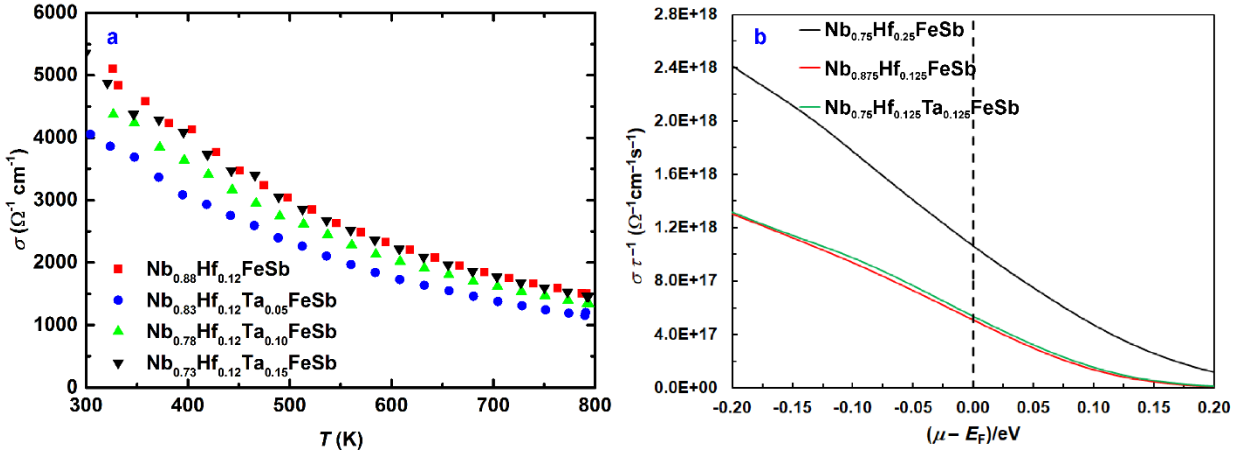

Figure 2. (**a**) Electrical conductivity of the $Nb_{0.88-x}Hf_{0.12}Ta_xFeSb$ ($0 \leq x \leq 0.15$) samples; and (**b**) calculated electrical conductivity over relaxation time (τ) against chemical potential at 300 K.

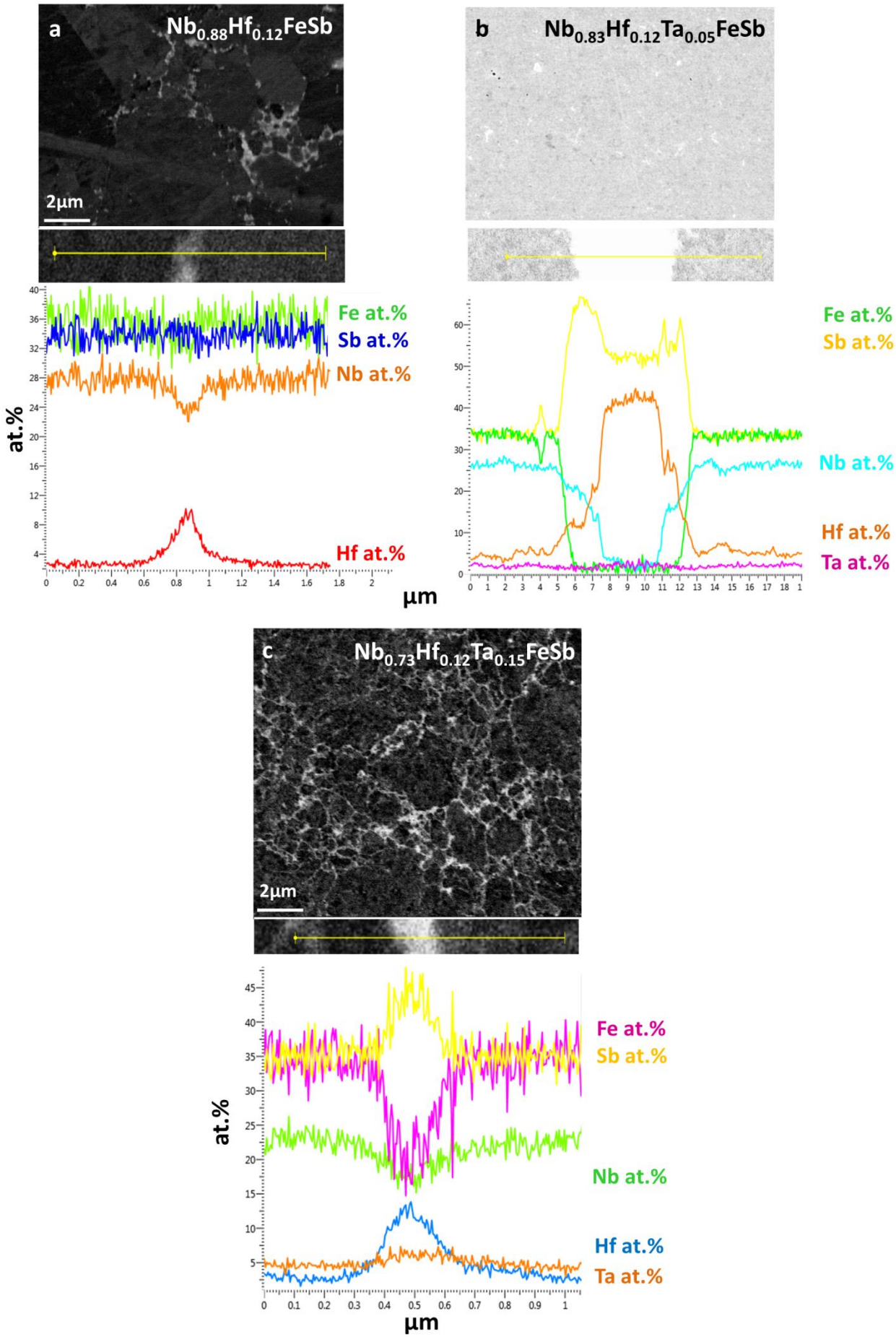
a
$Nb_{0.88}Hf_{0.12}FeSb$
2µm
Fe at.%
Sb at.%
Nb at.%
Hf at.%
at.%
µm
b
$Nb_{0.83}Hf_{0.12}Ta_{0.05}FeSb$
Fe at.%
Sb at.%
Nb at.%
Hf at.%
Ta at.%
c
$Nb_{0.73}Hf_{0.12}Ta_{0.15}FeSb$
2µm
Fe at.%
Sb at.%
Nb at.%
Hf at.%
Ta at.%
at.%
µm

Figure 3. SEM images and line scan analyses of Hf-rich regions and hafnium antimonide compounds at the grain boundaries observed in (**a**) $Nb_{0.88}Hf_{0.12}FeSb$, (**b**) $Nb_{0.83}Hf_{0.12}Ta_{0.05}FeSb$, and (**c**) $Nb_{0.73}Hf_{0.12}Ta_{0.15}FeSb$ samples.

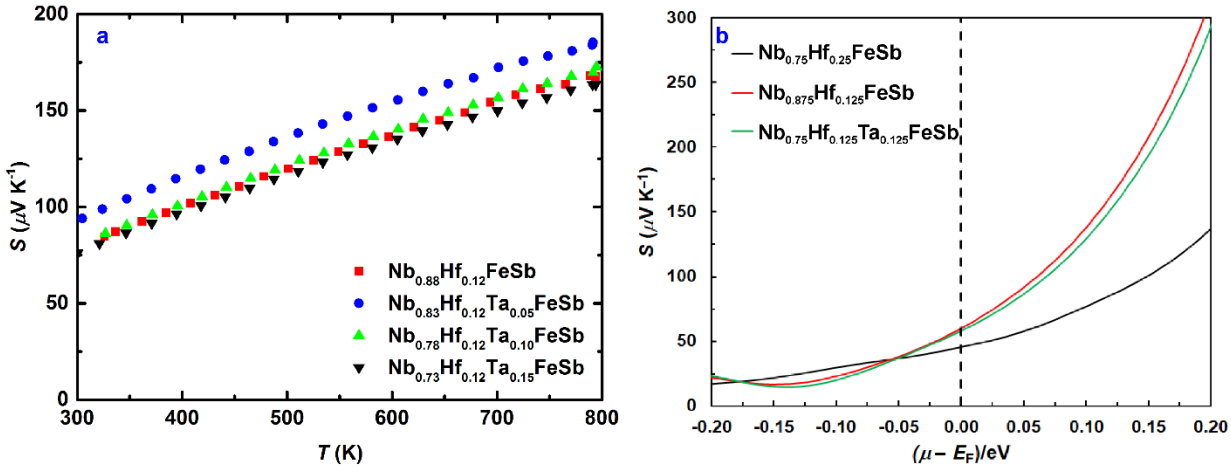

Figure 4. (**a**) Seebeck coefficient of the $Nb_{0.88-x}Hf_{0.12}Ta_xFeSb$ ($0 \leq x \leq 0.15$) samples; and (**b**) calculated Seebeck coefficient against chemical potential at 300 K.

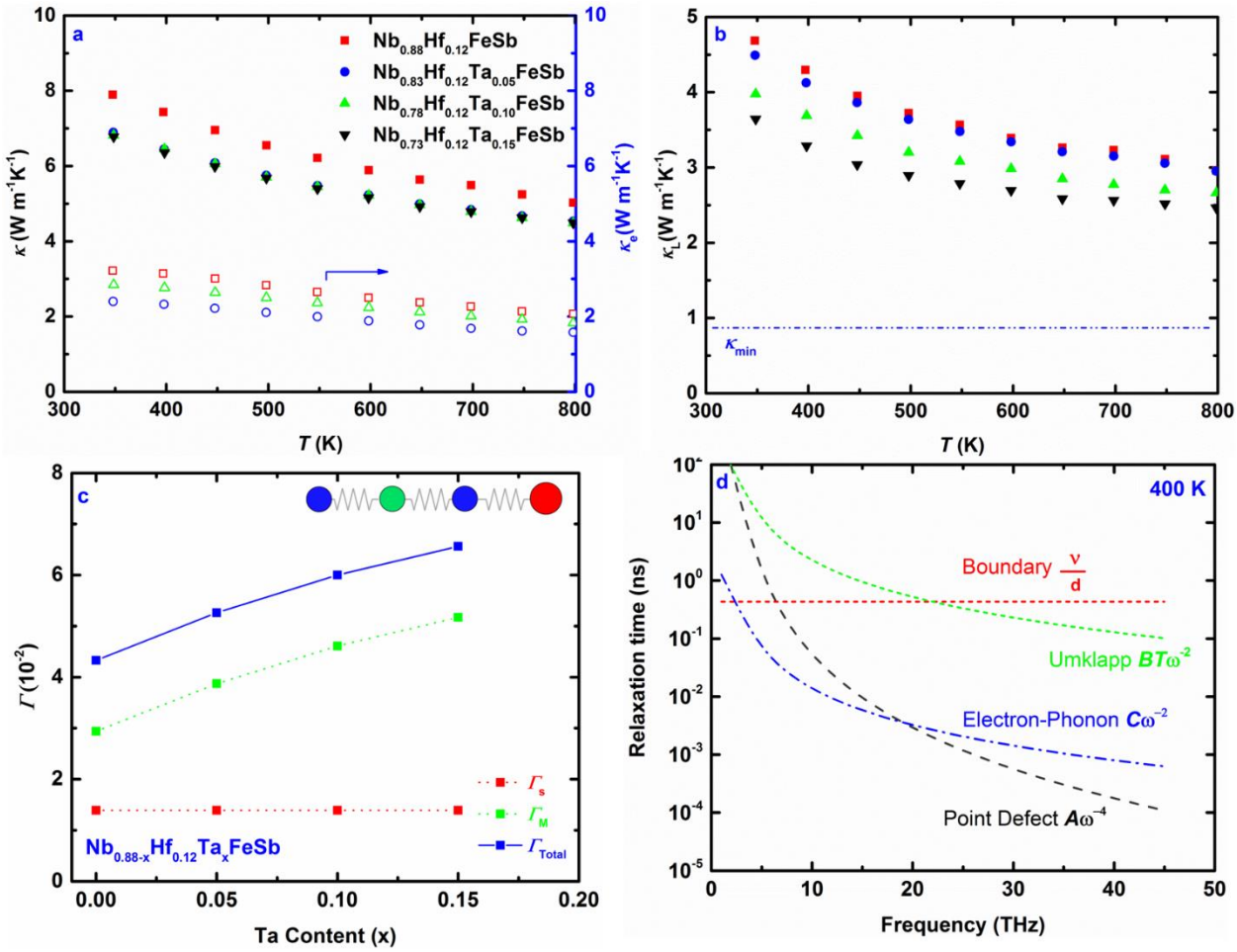

Figure 5. (**a**) Thermal conductivity (solid symbols), electronic part of thermal conductivity (open symbols); (**b**) lattice thermal conductivity of the $Nb_{0.88-x}Hf_{0.12}Ta_xFeSb$ ($0 \leq x \leq 0.15$) samples; (**c**) the calculated disorder parameter Γ for $Nb_{0.88-x}Hf_{0.12}Ta_xFeSb$ ($0 \leq x \leq 0.15$) samples, where Γ_M and Γ_s are mass and strain field fluctuations, respectively, and Γ_{total} is their sum ($\Gamma_{total} = \Gamma_M + \Gamma_s$);[48] and (**d**) phonon relaxation time against frequency at 400 K for $Nb_{0.73}Hf_{0.12}Ta_{0.15}FeSb$ sample.

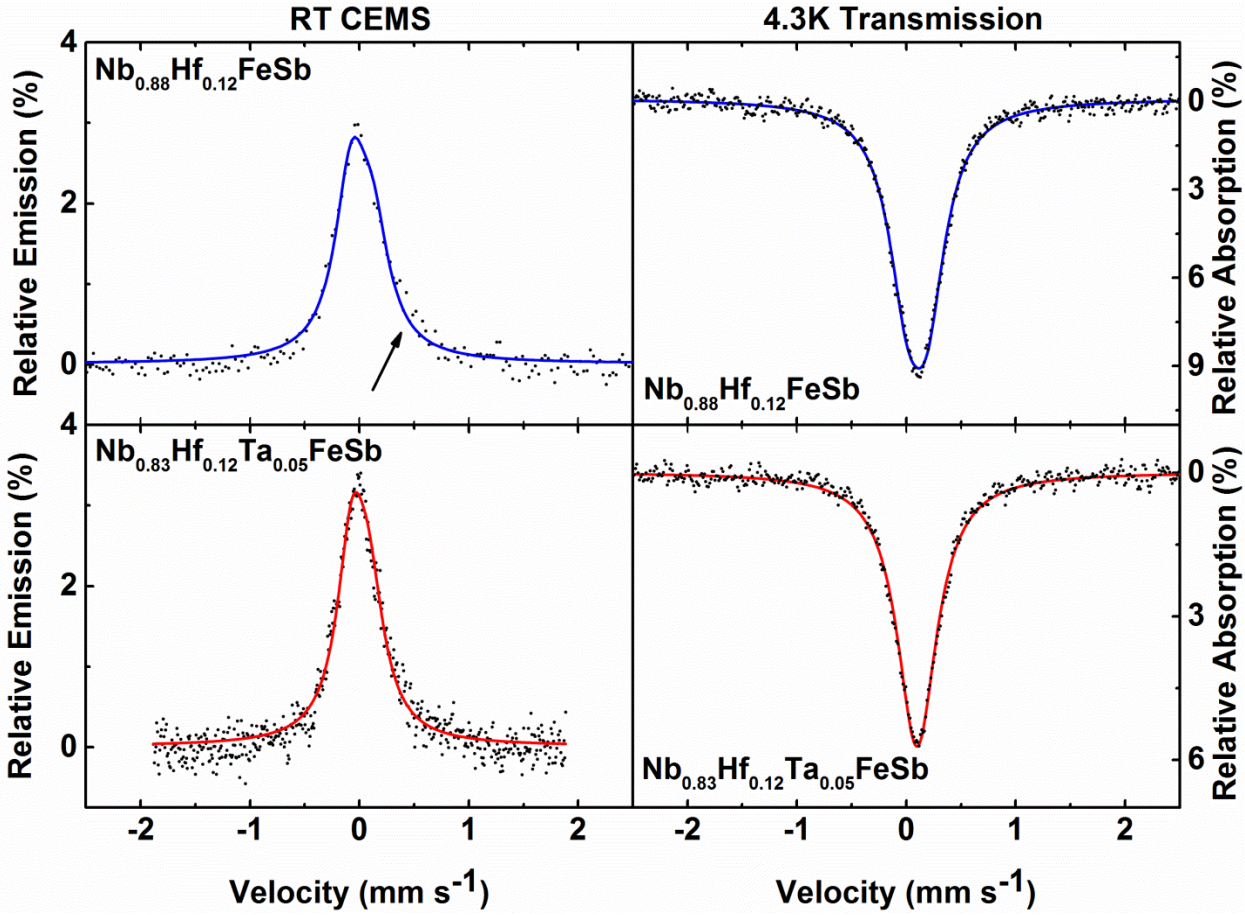

Figure 6. Mößbauer spectroscopy results for the $Nb_{0.88}Hf_{0.12}FeSb$ (blue) and $Nb_{0.83}Hf_{0.12}Ta_{0.05}FeSb$ (red) samples at room temperature (left) and 4.3 K (right), reproduced via a doublet of absorption lines, appearing as a single line due to the small quadrupole splitting.

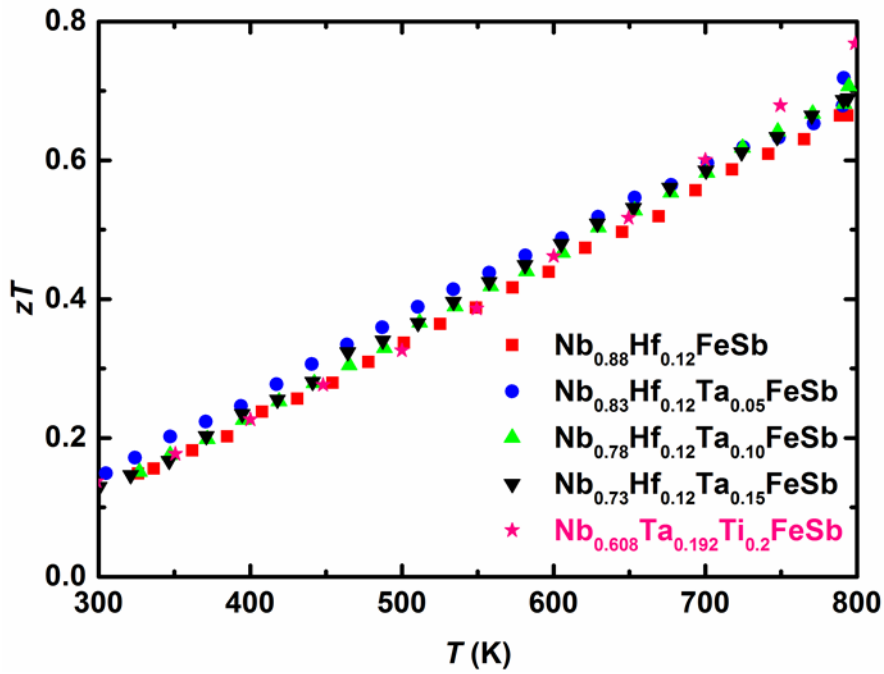

Figure 7. Temperature dependent dimensionless figure of merit of the $Nb_{0.88-x}Hf_{0.12}Ta_xFeSb$ ($0 \leq x \leq 0.15$) samples, compared with the $Nb_{0.608}Ta_{0.192}Ti_{0.2}FeSb$ sample (star symbol) reported by Yu et al.[21]

Table of Contents (TOC)